Recent advances in three-dimensional thin-film Li-ion batteries

S. Moitzheim[a], B. Put[a], P.M. Vereecken*[a,b]

[a]imec, Kapeldreef 75, B-3001, Belgium
[b]M2S department, KU-Leuven, Belgium
*Corresponding author: philippe.vereecken@imec.be

Introduction

Thin-film batteries for microstorage application

Historically, the introduction of the rechargeable Li-ion battery (LIB) was largely driven by the development of portable consumer electronics, such as cameras, mobile phones, and laptops.[1] Since their first successful commercialization in 1991 by Sony, LIBs have steadily been improving in terms of energy density and cost per watt-hour. Considerable improvements have also been made to their cycling stability, reliability and safety. Although many improvements have been made to LIBs over the years, it can be argued that the energy requirements of portable electronics have outgrown the capabilities of LIBs. While the size of the electrical components has been shrinking, the size of the battery has remained almost the same to meet application and consumer needs.

With the continuous miniaturization of electrical devices, in the so-called Internet-of-Things (IoT) era,[2] novel solutions for energy storage are necessary. Specifically, applications such as wearable electronics, implantable devices, and autonomous sensors are in need of specialized microstorage solution.[3] Currently, a main restriction to the form factor and size of these devices is the energy storage component. Unfortunately, shrinking the size of batteries always comes at the cost of storage capacity, as the capacity is directly proportional to the volume of the active battery components (the cathode and anode). To maximize the capacity, electrodes with high intrinsic volumetric capacity have to be used, while the number of "inactive" components (packaging, etc.) need to be minimized. Additionally, to solve the problem of limited energy available in a small volume—or even remove the need for external charging altogether—energy could be harvested from the environment, such as from light, vibration or heat.[3,4] Ideally, energy harvesters are integrated together with a microbattery to ensure that the energy produced can be stored when idle, and used during peaks in activity (e.g. when wirelessly transmitting data). To realize this, a microbattery that offers a large storage capacity in a small volume, and that can be charged/discharged quickly for many cycles is needed.

A type of battery that is considered ideal for miniaturization and fast charging, is the thin-film solid-state Li-ion battery (TFB) as shown in Figure 1a. In a TFB, the battery components are deposited as stacks of dense solid films. To enable this, a solid-state electrolyte (SSE) film is used as the physical separation between the positive and the negative electrode, which also provides Li-ion transport between the two. This is different to conventional LIBs, which use anode or cathode particles mixed with various additives (e.g. PVDF binder, carbon black) as the electrodes, while being soaked in a liquid electrolyte solution (see Figure 1b). A highly porous "separator" (typically polymeric) soaked with the electrolyte solution is used to prevent both electrodes from shorting. For TFBs, the electrodes (and the SSE) are typically in the thickness range up to a few micrometers, while for particle-based coatings this can be up to 100 μm in thickness.[5] Moreover, SSEs are more (electro-)chemically stable than solvent-based electrolytes, and have no issues with leakage or combustion, which make them generally safer to use.
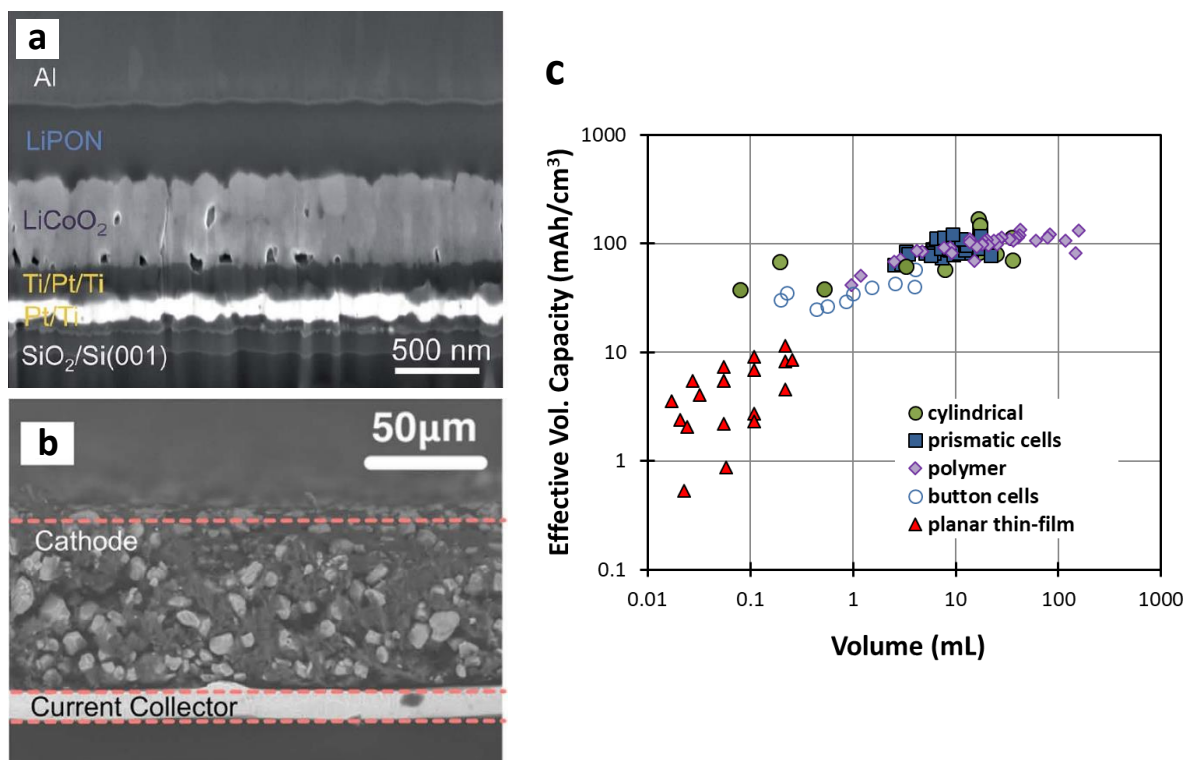
Figure 1. Comparison of TFBs and conventional particle-based batteries. Cross-section image of a TFB (a) and conventional powder-based LIB (b). In this example, the thin-film battery consists of a current collector (Pt/Ti), a cathode ($LiCoO_2$), an SSE (LiPON), and anode (Al). The conventional particle-based battery has a current-collector, cathode particles mixed with conductive carbon and binder additives, and a separator. Note the difference in total thickness between the particle and the thin-film coatings. (c) Comparison of effective volumetric capacities of commercial planar TFBs compared to conventional LIBs. (a) Adapted from ref. [6], copyright 2019 Royal Society of Chemistry. (b) Adapted from ref. [7] under CC BY 4.0 license.

Although the total electrode thickness is larger for conventional LIBs compared to TFBs, the size of individual electrode particles is in the same range as the film thickness in TFBs. This is related to the kinetics of Li-ion insertion. The particles are surrounded by the electrolyte soaking the porous electrodes, while carbon black acts as an internal electron conductor. The active electrode material consists of about 70% of the total electrode volume. On the other hand, TFBs can theoretically pack the electrodes more densely, and one would expect the volumetric energy density to be larger. However, even though the SSE film is thin, it still takes a relatively large fraction of total stack thickness: typically, the electrode/SSE ratio is about 1:10. For particle-based batteries where the separator is typically 10–20 µm thick, this ratio can reach 4:10. Practically, however, thin-film batteries show about an order of magnitude lower effective volumetric capacity (and energy density) compared to conventional particle based batteries (see Figure 1c). This is partially due to the relatively large fraction of inactive structural components (e.g. substrate, current-collectors, and packaging). Note that the relative contribution of the packaging is also the reason why button cells are lower in volumetric capacity. Unfortunately, the volume fraction of active materials in TFBs cannot be increased by depositing thicker electrode layers due to kinetic (i.e. low ionic and electronic conductivity) and structural (e.g. film delamination) reasons.

To increase the capacity of TFBs without significantly increasing the electrode film thickness, three-dimensional (3D) TFB are being considered. In this case, the capacity is increased by depositing a thin-film battery stack over a 3D micro-structured substrate.[8–11] The capacity is mainly enhanced by increasing the effective surface area of the 3D current-collector substrate. Note that the term "3D

2

battery" is also used more generally to describe a battery that has one or two 3D nanostructured electrodes. These often use nanoporous electrodes combined with a liquid electrolyte solution, such as the example from Pikul et al..[12] Although an interesting concept on its own, this is distinct from a 3D TFB, where a full thin-film solid-state battery stack is coated over a large surface area current-collector.

Unfortunately, 3D TFBs have proven technologically very challenging to realize. The promise of a high capacity and stable microbattery has yet to be realized. In this review, we discuss the recent advances of 3D TFBs and the challenges they are facing. In the first section, we determine what capacities can be expected from a theoretical point of view. For this we derive equations needed to determine the maximum capacity that can be achieved with 3D TFBs based on a regular array of micropillars. In subsequent sections, we review the latest results on the thin-film components—the cathode, anode and solid-state electrolyte—used to fabricate 3D TFBs. Finally, we discuss the recent developments in obtaining full 3D TFBs.

Basic components of thin-film Li-ion batteries

The main active components of a LIB are the two active electrodes which store Li-ions and electrons through electrochemical oxidation (anode) and reduction (cathode). An electrolyte between the cathode and anode prevents both electrodes from electrically shorting, and enables Li-ion transport between the two during operation. Li-ions and electrons are inserted and extracted from the electrodes. The electrons flow through the outer circuit and deliver power to the desired application, while the Li-ions flow internally through the electrolyte. The main driving force for the flow of electrons and subsequently Li-ions is the electrochemical potential difference between the cathode and the anode. Traditionally, the more positive electrode is referred to as the "cathode". The most widely employed cathode materials are $LiCoO_2$, $LiFePO_4$ and $LiMn_2O_4$ with respective electrode potentials of 3.8 V, 3.4 V and 4.1 V vs. Li^+/Li.[13] For the anode, typically specialty graphite with a potential of 0.1–0.2 V vs. Li^+/Li is used for high energy cells and $Li_4Ti_5O_{12}$ (1.5 V vs. Li^+/Li) for high-power applications.[13] A key reason for the high energy density of Li-ion batteries is that a large cell voltage (3 to 4 V) can be achieved using a combination of the above mentioned electrodes. Fast charging and discharging (power density) is achieved by the use of Li-ion as the insertion guest, which, due to its relatively small ionic radius and monovalent charge, offers relatively fast solid-state diffusion within the electrodes, as compared to other insertion guests (e.g. Na^+, K^+ or Mg^{2+}).[14]

As already mentioned, the size of active particles in conventional LIBs is in the same order as the film thickness of electrodes in TFBs. This is related to the fact that solid-state Li-ion diffusion is often the rate-limiting step during battery operation. To a first approximation, the characteristic time (τ) to fully charge an electrode limited by Li-ion diffusion can be given by:

$$\tau = \frac{l^2}{D}$$ (1.1)

with l the diffusion length (particle radius in LIBs or electrode thickness of TFBs, in m), and D the solid-state diffusion coefficient ($m^2 s^{-1}$). Taking, for example, the typical value of D for $LiFePO_4$ of about 1×10^{-16} $m^2 s^{-1}$,[15] and an electrode thickness of 1×10^{-6} m (i.e. 1 µm), gives a τ of about 3 h. Note that the actual ion mass transport is also governed by an additional migration component, the state of charge and the electrochemical gradient over the active material. Nevertheless, the characteristic diffusion time for Li-ions gives a good idea of the practical limit set by the thickness of the electrode films or particles radius. By scaling the electrode size to the nanometer regime (<100 nm), charging in a matter of seconds can be achieved.

3

Unfortunately, the use of nanostructures in commercial (liquid) LIBs has not yet been successfully introduced, since such systems are still too expensive and plagued by problems such as enhanced side-reactions, inter-particle resistance, agglomeration issues and low effective volumetric density.[16] On the other hand, for TFBs using a solid-state electrolyte, stability is greatly improved and interfaces can be controlled, which makes nanosizing perfectly viable for TFBs.

A major issue with planar TFBs, however, is that the total footprint capacity is limited, as only a relatively small electrode volume is available for energy storage. From the discussion above, it is understood that thicker electrode films cannot be used to increase the capacity due to kinetic restrictions. For conventional batteries, the electrode volume (and thus capacity) can easily be scaled by increasing the total thickness of the slurry-coated particle composite layer (i.e. increasing the active material "mass-loading"). The electrolyte solution penetrates the porous composite electrode layer and the electronic additive (e.g. carbon black) ensures electronic pathways throughout the electrode. For TFBs, another architecture needs to be used, which will be introduced in the next section.

Design aspects of three-dimensional thin-film batteries

To increase the footprint capacity of TFBs without increasing the electrode film thickness, the concept of three-dimensional (3D) TFBs is being investigated. Here, the capacity is increased by depositing the battery stack on a microstructured substrate.[8–11] In this case, the capacity is scaled by increasing the surface area of the 3D substrate. The substrate acts both as a support for the thin-film battery stack, as well as the electronic contact (current collector) to the first deposited electrode. The benefit of such a design is that the footprint capacity can be scaled by increasing the surface area, independent of film thickness. The concept is clarified in Figure 2. For the 3D TFB, relatively thin electrodes can be used for fast charge and discharge of the battery while the capacity is still high due to the area enhancement. For example, a 500 nm film is equivalent to a 15 micrometer planar film for an area enhancement with a factor 30.

Two important parameters govern the design of the 3D TFBs: the area enhancement factor (AEF) and the open volume (or effective porosity) of the 3D substrate. The AEF is the ratio between effective surface area of the 3D structure and its footprint (or geometric) area. Generally, the higher the AEF, the more capacity per footprint can be achieved. The open or free volume is the space available to host the full battery stack, and is important since it determines the maximum volume of the final battery stack and in turn achievable capacity. A larger free volume often comes at the cost of AEF, so a balance must be found to achieve the highest capacity.
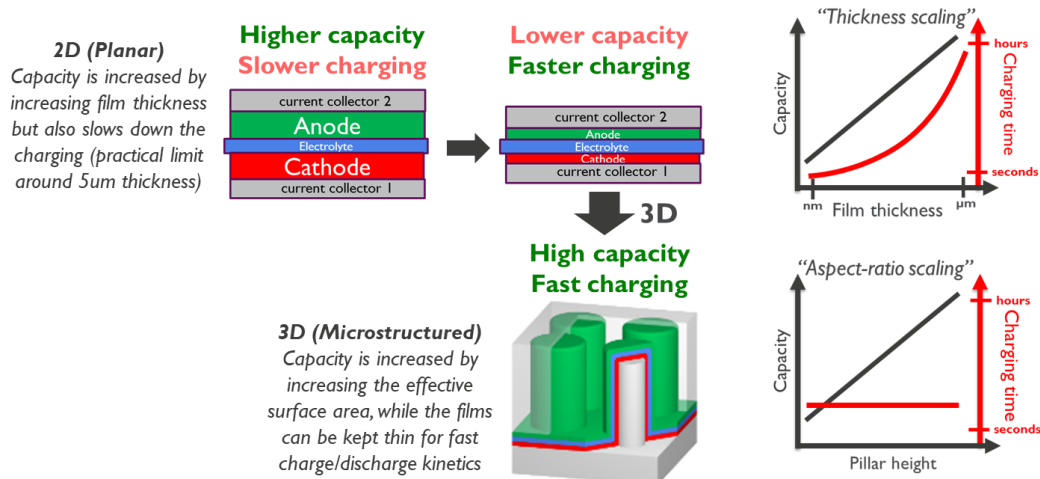
Figure 2. Scaling properties of planar and 3D thin-film batteries.

There are broadly two different classes of microstructures that can be considered as substrate for 3D TFB: periodic or aperiodic microstructures (see Figure 3). Periodic structures can, for example, be arrays of micropillars[17] or microtrenches.[18] Periodic structures often allow for a good control over the microstructure design, such as the amount of open volume and AEF, and are therefore ideally suited for the fundamental research into the fabrication and characterization of 3D TFBs. Also, such structures are typically more suited for conformal deposition of the various films in the battery stack.

Aperiodic structures, or in some cases termed "microsponges", can be made from carbonaceous materials such carbon nanotubes[19] and carbon nanosheets,[20] or from metals such as copper or nickel.[11] With aperiodic structures, higher AEFs are often achieved compared to the periodic structures, but typically it is more challenging to control the open volume or porosity of the structure. Also, depositing a full battery stack on such an aperiodic structure is generally more difficult than on a periodic one. A few examples using an aperiodic structure use a "hybrid" approach instead. (see e.g. ref. [21]). In this case, a separate substrate is used for each electrode, and combined like in a conventional LIB with a liquid electrolyte solution in between both 3D electrodes. Note that this is also often termed a "3D battery". Although it might theoretically be possible to fabricate a full 3D TFB on a single aperiodic scaffold, the realization of such a task may be still too far out of practical reach. For this reason, in this review we will focus on periodic 3D structures instead.
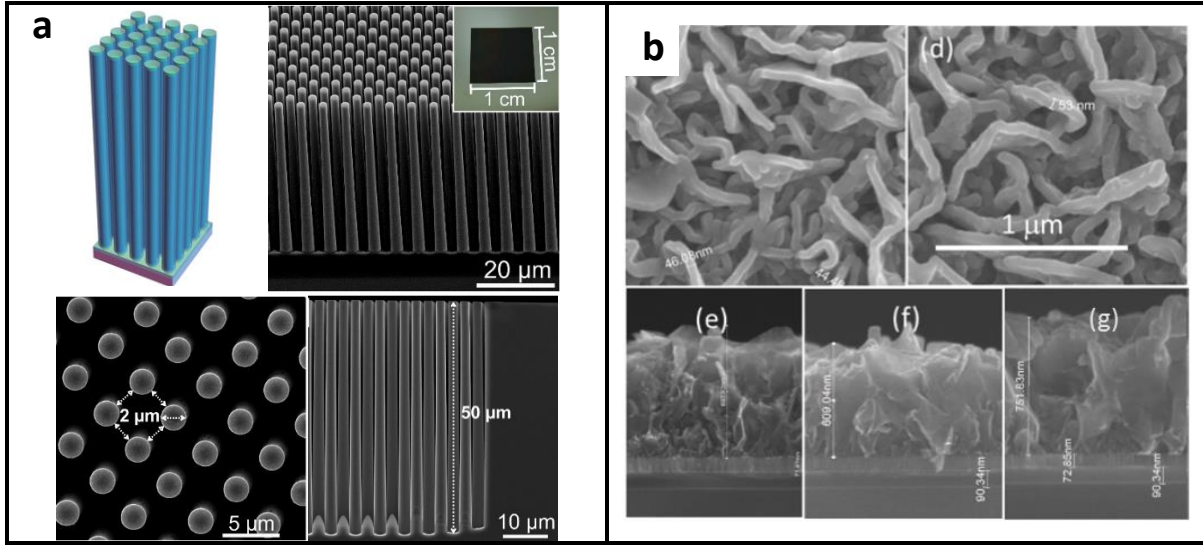
5

Figure 3. Example of periodic and aperiodic substrates for 3D TFBs coated by TiO₂. (a) Micropillar arrays were fabricated using photolithography and deep reactive ion etching of Si wafers. The pillars are arranged in a square lattice and used as a substrate for fabrication of 3D thin-film electrodes. Adapted with permission from [22]. Copyright 2019 American Chemical Society. (b) Carbon nanosheets deposited by CVD on a TiN-coated Si wafer, covered with TiO₂ deposited using ALD to form a 3D thin-film electrode. Adapted with permission from [23]. Copyright 2019 IOP Publishing.

Modeling the theoretical capacity of 3D TFBs

As a proof-of-principle, the theoretical achievable capacity of a 3D TFB based on a periodic micropillar structure is calculated in this section. Several reports have detailed the use of micropillar structures as substrate for 3D thin-film electrodes.[22,24–30] Micropillars are an excellent tool to develop and study 3D thin-film batteries, as they can be fabricated with relatively good control over the geometric parameters (height, diameter, inter-pillar spacing), and offer a wide range of aspect ratios (e.g. 1 to 200). Compared to microtrentches, micropillars offer some advantage as the more open space allows for easier deposition of the battery stack, as was shown in the case for vapor-phase deposition techniques such as atomic layer deposition (ALD).[31] However, one drawback compared to microtrenches is that free-standing pillar structures are more prone to breakage and collapse (especially when using liquid-phase deposition techniques). It is worth noting that the first functional 3D TFB was recently shown using a microtrench design,[32] as will be discussed further on.

Derivation of the optimal micropillar configuration

Before calculating the capacity for micropillar arrays, the arrangement (unit cell) of the micropillars needs to be defined. Figure 4 shows a top-view schematic of two different arrangements: the hexagonal (Figure 4a), and the (centred) square lattice (Figure 4) arrangement. By defining the unit cell using the pillar diameter (d) and inter-pillar spacing (s_p), the area of the unit cell can be given as:

$$S_{\text{hex}} = \frac{\sqrt{3}}{2}\left(d + s_p\right)^2 \text{ and } S_{\text{sq}} = \left(d + s_p\right)^2 \tag{1}$$

or more generally:

$$S_{\text{unit}} = G\left(d + s_p\right)^2 \tag{2}$$

with d and s_p in m, and G a constant related to the unit cell. For a hexagonal arrangement, $G = \frac{\sqrt{3}}{2} \approx 0.87$ and for a square lattice $G = 1$. Figure 4c gives a schematic of the cross-section of a full 3D thin-film battery stack. The pillar is coated with a first electrode (l_1, e.g. cathode), solid-state

electrolyte (l_{sse}), and second electrode (l_2, e.g. anode). The footprint capacity (C_{3D}) of the 3D electrode stack can be determined by calculating the volume of l_1 per area of the pillar unit cell:

$$C_{3D} = C_v \cdot \frac{V_{el}}{S_{unit}} = C_v \cdot \frac{V_{2D} + V_{pil}}{S_{unit}} = C_v \frac{l_1 G(d+s_p)^2 + \pi h l_1 (d+l_1)}{G(d+s_p)^2} = C_v l_1 \left[1 + \frac{\pi h(d+l_1)}{G(d+s_p)^2} \right] \quad (3)$$

Here, V_{el} (m^3) is the total volume of active electrode material in the pillar unit cell, S_{unit} (m^2) the footprint area of this cell and C_v (Ah cm^{-3}) the volumetric capacity of the active electrode material. Note that it is assumed that the first electrode is the capacity determining electrode. In eq. 3, V_{el} is separated into a planar part, V_{2D}, which is the volume of the electrode on the top and at the bottom in-between the pillars, and a vertical part, V_{pil}, which is the volume of the electrode attached to the pillar. For tall pillars ($h \gg l_1$), the contribution of V_{2D} to the total capacity is negligible.
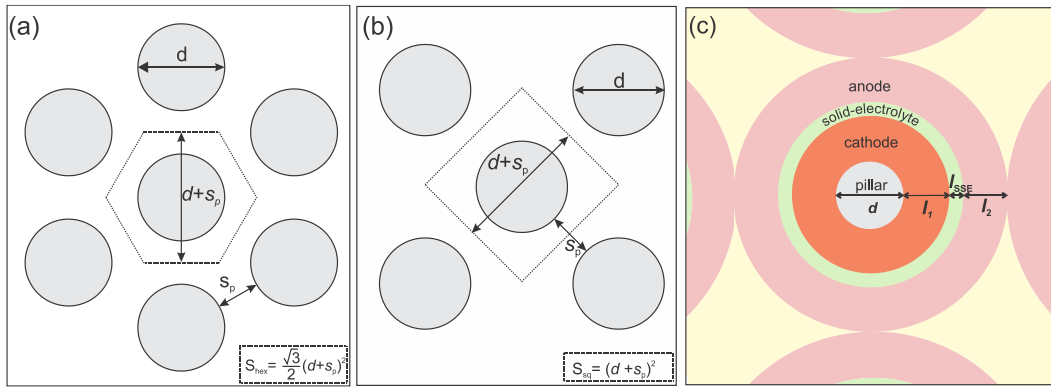

Figure 4. Top view of a pillar array arranged in a hexagonal lattice (a) and a centered square lattice (b). The diameter d, and spacing s_p, are indicated, together with the unit cell (dotted lines). (c) A cross-section schematic of the 3D thin-film solid state battery. Pillars arranged in a square lattice are coated with a cathode (l_1), solid-electrolyte (l_{sse}) and anode (l_2).

Eq. 3 can be divided by the final storage device thickness which includes packaging, substrate support and height of the 3D structure:

$$C_{3D,v} = C_v \frac{l_1 G(d+s_p)^2 + \pi h l_1 (d+l_1)}{(h+p) G(d+s_p)^2} \quad (4)$$

where p (m) is the sum of the packaging substrate and support thickness.

Equation 3 is plotted in Figure 5a-c to show the dependence of the footprint capacity on the different parameters for three specific inter-pillar spacings (1, 2 and 5 µm). For all calculations, we assumed an active electrode volumetric capacity (C_v) of 1000 mAh cm^{-3}. We have shown previously that such capacity can be achieved with 100 nm thick films of Cl-doped am-TiO$_2$ as the negative electrode[22] and LiMn$_2$O$_4$ as the positive electrode.[33] In Figure 5a, the footprint capacity is calculated as a function of pillar height. The capacity depends linearly on the pillar height, analogous to increasing the equivalent thickness with planar thin-film batteries. Figure 5b shows the footprint capacity as a function of pillar diameter. As shown in Figure 5a, a smaller inter-pillar spacing leads to a higher capacity. Interestingly, for each spacing, a maximum in capacity is obtained.

For example, for a 1 µm spacing, the capacity is at maximum when the pillar diameter reaches 0.6 µm. The effect can be understood by an increase in active material volume for larger pillar diameters, which is counter-balanced by a decrease in pillar density (i.e. number of pillars per area).

7

The optimal (d_{opt}) diameter is found by maximizing eq. 3 and solving $\frac{dC_{3D}}{dd} = 0$, which leads to:

$$d = d_{\text{opt}} = s_p - 2l_1 \tag{5}$$

Combining eq. 3 with eq. 5 leads to the footprint capacity using an optimal pillar diameter ($Q_{3D,\text{opt}}$):

$$Q_{3D,\text{opt}} = C_v l_1 \left[1 + \frac{\pi h}{4G(s_p - l_1)} \right] \tag{6}$$

In this optimized case, the footprint capacity becomes independent on the pillar diameter. To further optimize eq. 6, a minimum for the spacing (s_p) needs to be found, which will be shown below. Returning to Figure 5c, the capacity as a function of electrode thickness is shown for different spacings. As a reference, the theoretical capacity of a thin-film battery with planar geometry is added, which is clearly outperformed by the 3D structured electrode. The inter-pillar spacing (and thus pillar density) defines the electrode thickness required to reach a certain desired capacity. Since the film thickness largely influences the rate-performance, a small spacing is ideal for high capacity and ultra-fast charging microbatteries. However, the thickness of the full stack can never exceed half the spacing, and thus a maximum capacity is reached at a certain thickness in Figure 5c (denoted by the square, triangle and circle symbols).

(a)   (b)   (c)
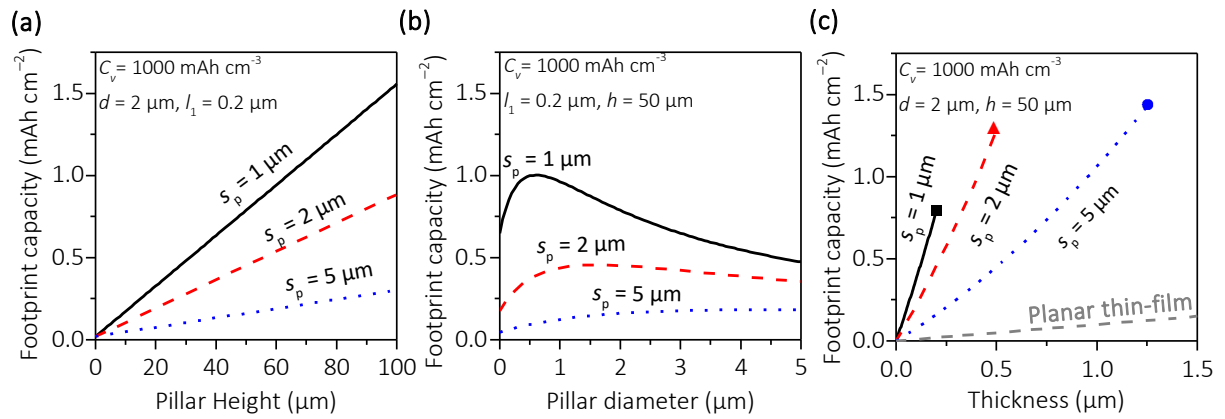

Figure 5. Theoretical capacity calculations (using eq. 3) of different micropillar designs. (a) The influence of pillar height, (b) pillar diameter and (c) first electrode thickness are shown for different values of spacings. Micropillars are arranged in a square lattice (*G* = 1). The maxmim electrode thickness is 0.25 (black square), 0.5 (red triangle) and 1.25 (blue circle) μm, for 1, 2 and 5 μm spacing, respectively. The corresponding volumetric capacity (*C_v*), electrode thickness (*l_1*), pillar diameter (*d*), and pillar height (*h*) used for the simulations are shown in the insets.

Minimizing the inter-pillar spacing and second electrode thickness

To understand the ultimate limit of the micropillar configuration, the smallest possible inter-pillar spacing must be determined. If the spacing is such that it contains twice the full battery stack exactly, the following relationship holds (see also eq. 5):

$$s_p = 2(l_1 + l_{\text{SSE}} + l_2) = d_{\text{opt}} + 2l_1 \tag{7}$$

Where l_{SSE} is the solid-electrolyte thickness (m) and l_2 is the second electrode thickness (m). For the solid-electrolyte film, the thickness is ideally as thin as possible, provided it can be made free of pinholes and does not physically break down (chemically, ionically, or electronically). Note that we neglect the thickness of the second current collector as it can be filled inside the voids next to the pillars. The second electrode thickness (l_2) will depend on its volumetric capacity, and the thickness (or volume) and volumetric capacity of the first electrode. Even if both electrodes (anode and cathode) have the same volumetric capacity, simply based on geometric considerations, their thickness will be different. Since the perimeter of the outer electrode film is larger than the inner electrode, a smaller

8

thickness will lead to the same volume and in turn capacity. Ideally, the electrode with the lowest intrinsic rate-performance is chosen as the (thinner) second electrode, as this would enhance its rate-performance. When the electrodes are chosen to be capacity matching, the following relationship holds:

$$C_v V = C_{v,2} V_2 \rightarrow \frac{C_v V}{C_{v,2} V_2} = r_{cc} \cdot \frac{V}{V_2} = 1 \tag{8}$$

where C_v and V, and $C_{v,2}$ and V_2 are the volumetric capacity (Ah m^{-3}) and electrode volume (m^{-3}) of the first and second electrode, respectively, and $r_{cc} = C_v/C_{v,2}$. As an approximation, we only consider the volume attached to the vertical perimeter of the pillar, since the volume of the layers on top and in-between the pillars will be negligible compared to the total volume (for $h \gg l$). Introducing the volume of the electrodes attached to the pillars in eq. 8 leads to:

$$r_{cc} \frac{\pi h l_1 (d+l_1)}{\pi h l_2 (l_1 + d + l_{sse} + l_2)} = r_{cc} \frac{l_1(d+l_1)}{l_2(l_1+d+l_{sse}+l_2)} = 1 \tag{9}$$

After each consecutive layer, the perimeter of the pillar structure increases. The minimum thickness of the second electrode (l_2) can be found by solving eq. 9 for l_2, resulting in:

$$l_2 = \frac{1}{2}\left[\sqrt{4 r_{cc} l_1(d+l_1) + (d+l_1+l_{sse})^2} - (d+l_1+l_{sse})\right] \tag{10}$$

Next, eq. 10 can be introduced into eq. 7, and solved for d_{opt}:

$$d_{opt} = 2(l_{SSE} + l_2) = 2\left(l_{SSE} + \frac{1}{2}\left[\sqrt{4 r_{cc} l_1(d_{opt}+l_1) + (d_{opt}+l_1+l_{sse})^2} - (d_{opt}+l_1+l_{sse})\right]\right)$$

$$\rightarrow d_{opt} = \frac{1}{6}\left[-2l_1 + 4 r_{cc} l_1 + 6 l_{SSE} + \sqrt{(l_1(2-4r_{cc}) - 6l_{SSE})^2 + 48 l_1(r_{cc}\, l_1 + l_{SSE})}\right] \tag{11}$$

Finally, by introducing eq. 7 and 11 into eq. 6, a (long) equation for the optimized theoretical footprint capacity can be found, which depends only on l_1, r_{cc}, l_{sse}, C_v, h and G. Interestingly, l_2 and s_p are fixed by the choice of these parameters. The results of these optimization studies were recently published and are shown in Figure 6.[34] Here, the capacity is plotted as a function of h and l_1, with $C_v = C_{v,2} = 1000$ mAh cm^{-3}, $l_{sse} = 100$ nm and $G = 1$.

Figure 6 reveals that a high capacity can achieved in two different ways: increasing the aspect ratio (and the pillar density) or increasing the film thickness. Inherently, this also shows that there is a trade-off between faster charging speed (i.e. using thinner films with high AR) and lower technological complexity (i.e. when using "thick" films with low AR). It is therefore conceivable that different design would be used depending on whether the application needs fast charging capability or not. The next step is to combine these models with experimental values of volumetric capacities as a function of electrode thickness and charging rate. Analogous to the historical development of transistors (see Moore's law), the roadmap for such 3D thin-film batteries will be the continuous increase in pillar density to enhance the (charging) speed.
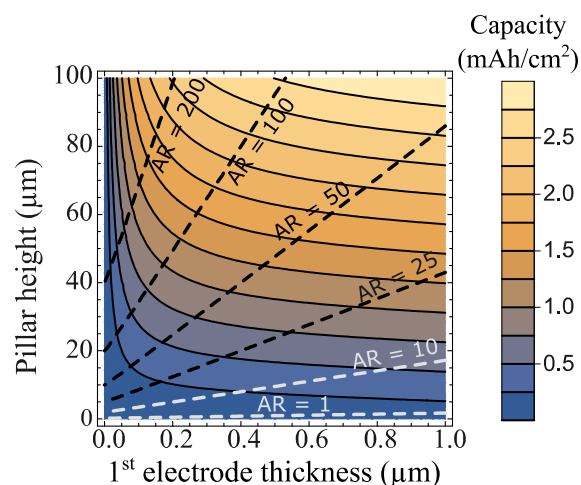
Figure 6. Theoretical calculations of the maximum footprint capacity for 3D micropillar arrays arranged in a square lattice (G = 1). A 100 nm solid-electrolyte, and electrodes with equal volumetric capacity (1000 mAh cm^{-3}) are assumed. Dotted lines denote the corresponding aspect ratio (AR = h/d) of the pillar structure. Adapted with permission from [34]. Copyright 2019 American Chemical Society.

State-of-the-art 3D thin-film electrodes

There are various methods available to deposit thin-film on microstructure current collectors. For example, techniques such as chemical solution deposition (CSD),[35] electrochemical deposition (ECD),[36,37] and atomic layer deposition (ALD),[22,32,38] have been shown to produce conformal films on periodic 3D current collectors. Important for the fabrication of a full 3D TFB stack, is that consecutive deposition techniques are compatible with the underlying materials. In the following section, state-of-the art 3D thin-film electrodes are discussed, without taking into account whether the reported fabrication technique would be feasible in a full 3D thin-film battery. Another important aspect to consider is the conformality that has actually been achieved. Unfortunately, a detailed analysis of the thin-film conformality across a 3D substrate is rarely reported for 3D TFB electrodes. Also, many focus on the deposition technique, whereas the electrochemical activity and capacitance of the films is not always reported. Nevertheless, in the following sections we discuss recent developments in 3D thin-film cathodes and anodes.

Cathodes

Historically, LiCoO$_2$ has been the most successful insertion electrode material in commercial LIBs. Its good cycle life, high rate-performance and practical capacity of 140 mAh g^{-1} (about 700 mAh cm^{-3}), have made it an excellent cathode choice. A planar TFB consisting of 4 μm of LiCoO$_2$ with a LiPON SSE of and metallic Li as anode has shown a reversible capacity of about 250 μAh cm^{-2} with a current density of 200 μA cm^{-2}.[39] It is likely that further increasing the thickness would increase the capacity. On the other hand, this would likely come at a penalty of rate-performance. Such a planar TFB is a good comparison point for 3D TFBs; at least capacities several times higher than 250 μAh cm^{-2} with comparable or preferably better rate-performance than the planar competition are needed. Note that for the commercially available TFB products of Fig. 1c, the footprint capacity varies between 40 and 200 μAh cm^{-2}, with footprint current densities between 0.2 and nearly 8 mA cm^{-2}.

Looking at different cathode materials, lithium nickel manganese cobalt oxide-type cathodes (e.g. LiNi$_{1/3}$Mn$_{1/3}$Co$_{1/3}$O$_2$) are being used more recently in commercial LIBs. These offer a higher capacity (>160 mAh g^{-1}) at reasonable rate-performance and stability. To increase capacity and decrease cost, the current trend is to increase the Ni content while reducing the Co and Mn contents, which however comes at the cost of stability.[40]

For periodic 3D TFBs, different cathode materials have been investigated. Arguably, it is rather challenging to deposit functional $LiCoO_2$ and $LiNi_{1/3}Mn_{1/3}Co_{1/3}O_2$ on 3D structured substrates. An important drawback of these materials is the high annealing temperature (> 450 °C) required to obtain the active crystal structure (see e.g., refs. [33] and [39]). This leads to significant challenges for the underlying current collector, which loses its electrical conductivity as a result of oxidation. Hence, electrodes that can be deposited using "mild" conditions (e.g. 100—200 °C) are receiving increased interest in recent years. In several cases, ALD was shown as a viable technique that offers conformal and good quality films (i.e. film roughness and chemical composition), while offering such mild deposition conditions. In a few cases, it has even been shown that amorphous electrode films deposited by ALD offer enhanced Li-ion insertion properties.[41–43] Although ALD offers a rather slow deposition rate, the benefit of having high quality and conformal thin-film electrodes have made ALD a popular choice for fabricating 3D thin-film electrodes. Still, the thickness of the ALD layers are typically below 30 nm as otherwise the deposition time becomes too long. Unfortunately, the footprint capacity of such 3D electrodes cannot match that of planar thin-film batteries and thus have so far only academic importance.[25,27,44,45]

A summary of 3D thin-film cathodes deposited on periodic 3D current-collectors is shown in Table 1. For this overview, thin-films deposited on aperiodic current-collectors were omitted. As can be seen from Table 1, most 3D thin-film cathodes consist of Li-free films deposited by ALD (i.e. V_2O_5, VO_2, and $FePO_4$). The highest footprint capacity for a Li-free 3D electrode was 130 µAh cm^{-2} (at a rate of 0.7 C, where the "C-rate" is the applied current divided by the maximum capacity), using amorphous VO_2 deposited by ALD on Si-based micropillars (see Figure 7a).[43] In this case, a Pt/TiN coated Si micropillar array was used with an AEF of 21. Remarkably, rate-performance experiments showed that still about 40% of the capacity was accessible at a rate of 40 C (50 µAh cm^{-2}). Note that the use of "Li-free" cathodes in full 3D TFBs means that either a lithiated anode needs to be used, or that the cathode needs to be lithiated after deposition. For example, Pearse et al. deposited V_2O_5 by ALD and then lithiated the electrode in a liquid based electrochemical cell before subsequent deposition of the final battery layers.[46] Ideally, a lithium-containing cathode film would be directly deposited instead.

Besides a $LiCoO_2$ film deposited by spray coating on Al nanorods, to our best knowledge there are no reports of lithium-containing cathode films that can be deposited conformally and have been measured electrochemically. In our group, we have developed a process for conformal coating of $LiMn_2O_4$ by thin-film solid-state reaction (SSR) between conformal MnO_2 and Li_2CO_3 films.[47,48] The MnO_2 films are deposited by electrochemical deposition (ECD) where excellent conformality is obtained due to the resistive nature of the MnO_2.[36,49] Alternatively, conformal MnO_2 (and MnO) films can also be obtained by ALD.[50] Using 3D ECD MnO_2 films converted to $LiMn_2O_4$, already a footprint capacity of 500 µAh cm^{-2} is shown for a 350 nm thin film. With the ECD process, MnO_2 films of micrometer thickness were shown possible[36] and thus capacities over 1 mAh cm^{-2} are feasible. However, only the 3D electrode with 350 nm thick $LiMn_2O_4$ was demonstrated so far. Next the integration of a full thin-film stack for demonstration of a 3D TFB is needed. The advantage of $LiMn_2O_4$ over $LiCoO_2$ is its cubic spinel structure, which means that crystal orientation is not an issue as for the layered rock salt structure. Disadvantage of $LiMn_2O_4$ is its much lower electronic conductivity than $LiCoO_2$ (10^{-6} vs. 10^{-4} S cm^{-1}).[51]

Table 1. Comparison of 3D thin-film cathodes reported in literature.

| Electrode Material	3D current-collector	AEF	Low-rate Capacity ($\mu Ah\ cm^{-2}$)	High rate capacity ($\mu Ah\ cm^{-2}$)	Details	Ref.
$LiCoO_2$	Al nanorods	10	120 (C/5)	80 (8 C)	30 nm $LiCoO_2$ by spray coating	[44]
V_2O_5	Nanostructured micropillars	7.5	38 (C/3)	25 (4 C)	30 nm V_2O_5 by ALD	[25]
VO_2	Pt/TiN-coated Si micropillars	21	130 (0.7 C)	50 (40 C)	50 nm of amorphous VO_2 by ALD	[43]
$FePO_4$	Pt-coated Si micropillars	21	20 (1 C)	6 (90 C)	33 nm of amorphous $FePO_4$ by plasma enhanced ALD	[27]
$LiMn_2O_4$	Ni-coated Si micropillars	21	500 (C/10)	300 (10 C)	350 nm ECD MnO_2 converted to $LiMn_2O_4$ by SSR with ALD Li_2CO_3 film	[48]
TiP_2O_7	Si micropillars	7.4	-	-	80 nm TiP_2O_7 by plasma enhanced ALD*	[30]

*The footprint capacity was not reported
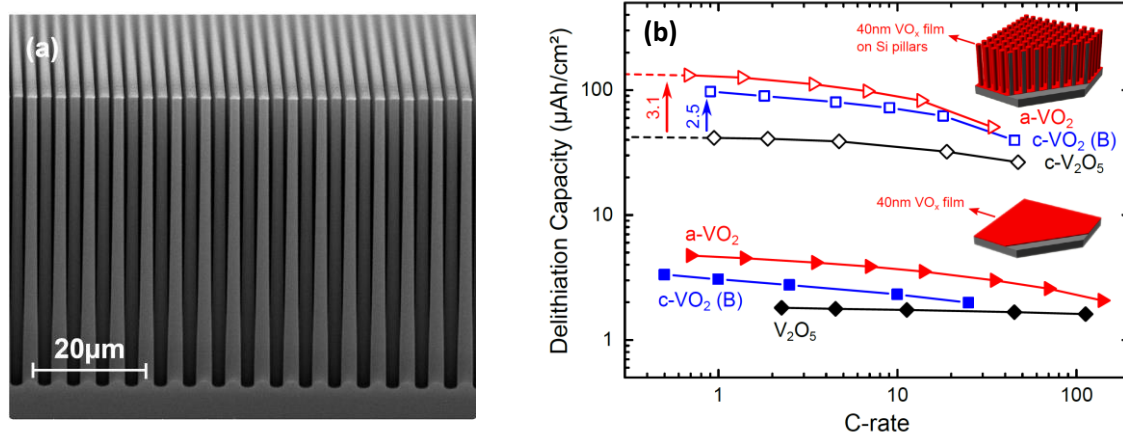
Figure 7. (a) Pt/TiN- Si-micropillar array coated by a VO_2 film. (b) Rate capability for planar and micropillar electrodes coated with 40 nm amorphous VO_2 (red), and crystalline VO_2(B) (blue) and V_2O_5 (black). Adapted with permission from [43]. Copyright 2019 American Chemical Society.

Anodes

One of the most successful anode materials in conventional LIBs is graphite. It gives a low electrochemical potential, high gravimetric capacity and good stability. Unfortunately, it has a rather mediocre volumetric capacity (i.e. 790 mAh cm^{-3}), and suffers from a relatively large volume expansion, limiting its application for TFBs. Furthermore, the fabrication of graphite thin-films is mainly performed by chemical vapor deposition (CVD), which is less suited for conformal deposition on high-aspect ratio structures. Moreover, conventional CVD of graphite requires temperatures of around 1000 °C, which brings considerable challenges to its integration in the full stack. Alternatively, plasma-enhanced CVD can be used to lower the deposition temperature,[52] but this typically decreases the capability for conformal coating. Therefore, although graphite is the most successful anode for conventional LIBs, it is not so successful as a 3D thin-film electrode. Similarly, the use of conversion or alloying anodes (e.g. Si or Ge) might find limited use in 3D TFBs, as their large volume expansion upon Li-ion insertion will lead to significant issues with film cracking (see e.g. [53])

delamination and internal short circuiting. For example, polycrystalline Si films were deposited on TiN-coated microholes and the electrochemical performance was measured.[54] A capacity of 255 µAh cm^{-2} was obtained, but which quickly faded within 20 charge/discharge cycles. Although alloying electrodes have an intrinsically high capacity, issues with their stability and volume expansion make them a less ideal candidates for 3D TFBs.

Fortunately, there are alternative thin-film electrode materials available that have shown a high and stable capacity, and that can insert Li-ions at sufficiently low enough potentials to make them suitable as anodes. A variety of thin-film electrodes, such as TiO_2,[41] MoO_2,[55] Nb_2O_5,[56] and $Li_4Ti_5O_{12}$[57] have shown excellent electrochemical properties. Although a plethora of thin-film anodes have been shown in planar configuration, the list of 3D thin-film anodes deposited on periodic 3D current collectors is rather limited (see Table 2). Monolithic 3D electrodes (e.g. TiO_2 nanotubes) or so-called 3D ordered macroporous (3DOM) electrodes were omitted as they are not thin-film electrodes but rather 3D nano-electrodes (e.g. see refs. [21,58,59]).

Table 2. Comparison of 3D thin-film anodes reported in literature.

Electrode Material	3D current-collector	AEF	Low-rate Capacity (µAh cm^{-2})	High rate capacity (µAh cm^{-2})	Details	Ref.
TiO$_2$	Al nanorods	10	11 (C/5)	3.9 (20 C)	17 nm TiO$_2$ by ALD	[60]
	Al nanorods	20	25 (C/10)	5 (10 C)	15 nm TiO$_2$ by ALD	[61]
	Pt-coated Si microtubes	25	200 (C/10)	25 (4 C)	150 nm TiO$_2$ by ALD	[26]
	TiN-coated Si pillars	7.4	8 (C/5)	3 (3.5 C)	40 nm TiO$_2$ by LPCVD	[28]
	Pt/Al$_2$O$_3$-coated Si microtubes	53	370 (C/16)	75 (2 C)	Li$_3$PO$_4$-coated 155 nm TiO$_2$ by ALD	[38]
	TiN-coated Si pillars	21	242 (C/4)	89 (20 C)	100 nm Cl-doped amorphous TiO$_2$ by spatial ALD	[22]
Li$_4$Ti$_5$O$_{12}$	TiN-coated Si pillars	21	-	-	Conformal Li$_4$Ti$_5$O$_{12}$ via ECD and solid-state conversion.*	[37]
	TiN-coated Si pillars	7.4	-	-	MOCVD of Li$_4$Ti$_5$O$_{12}$*	[62]
WO$_3$	TiN-coated Si pillars	7.4	21 (C/2)	3 (2 C)	30 nm WO$_3$ by ultrasonic spray deposition	[35]
Si	TiN-coated microholes (in Si)	7.1	255^x (C/10)	-	56–31 nm Si by LP-CVD	[54]

*The footprint capacity was not reported or could otherwise not be extracted
^{x}Only about 20% of the capacity remained after 50 charge/discharge cycles

From Table 2, it is clear that the most widely reported 3D thin-film electrode is TiO$_2$. Due to its high theoretical volumetric capacity of 1280 mAh cm^{-3}, TiO$_2$ is an interesting candidate as it offers a small volume expansion and high cycling stability.[63,64] Furthermore, there are a wide range of ALD processes available for the deposition of TiO$_2$ and the material is well-known from semiconductor industry. From Table 2, the highest footprint capacity for a 3D thin-film anode was achieved by Létiche et al.,[38] who combined a Si-microtube array (AEF of 53) with 155 nm of TiO$_2$ and covered it with a Li$_3$PO$_4$ SSE film. They obtained 370 µAh cm^{-2} at a rate of C/16. Unfortunately, only about 20% was accessible at a relevant rate of 2 C. A slightly lower footprint capacity was achieved using chlorine-doped TiO$_2$ deposited on Si pillars (242 µAh cm^{-2}), but in this case about 80% was accessible at 2 C and even still 37% was accessible at a rate of 20 C.[22] The better rate-performance was attributed to the inherently faster Li-ion kinetics as a result of chlorine doping. This illustrates that is not only it important to use a high AEF with sufficiently thick electrodes, but an intrinsically high-rate performance electrode material needs to be used as well.

As can be seen in Table 2, most anode thin-films were deposited by atomic layer deposition (ALD) and (low-pressure) chemical vapor deposition (LP-CVD). A variety of other anode materials can be deposited by ALD, such as Li$_4$Ti$_5$O$_{12}$,[65] Nb$_2$O$_5$[66] and MoO$_2$,[67] which, however, were not electrochemically tested as 3D TFB electrode to date.

Conformal solid-state electrolytes

One of the most crucial components of the 3D TFB is the solid electrolyte. This layer provides electrical insulation between the anode and cathode, while facilitating Li-ion transport. The conformality and thickness uniformity of this material is critical for a uniform resistance over the whole stack. Moreover, a single pinhole will short-circuit the cell, rendering it useless. Therefore, an adequate thickness that guarantees its proper functioning must be chosen. On the other hand, the layer itself does not contribute to the energy density of the cell, so any reduction in its thickness will thus result in an increased energy density.

Currently, numerous materials with a wide range of Li-ion conductivities are known; a comprehensive review of recent findings can be found in ref. [68]. Conductivities for solid state Li-ion electrolytes range from 10^{-9} to 2×10^{-2} S cm^{-1}. Each of them has specific advantages and drawbacks and typically a trade-off between (electro)chemical stability and ionic and electronic conductivity has to be made. Note that for 3D thin film batteries, the requirements for the ionic conductivity are less stringent as the thin film nature will greatly reduce the ionic resistance. For example, the ionic resistance for an electrolyte of 50 μm thickness with a conductivity of 10^{-7} S cm^{-1} will be the same as that of one with a conductivity of 10^{-9} S cm^{-1} and a thickness of 500 nm.

Even though there is a wide range of solid electrolytes known, for most of these materials no conformal deposition technique is available. As it is described above, the aspect ratio of the 3D microstructures (e.g. the length of the micropillars) largely determines the eventual battery capacity. Even though depositions of SSEs using physical vapor deposition (PVD) and CVD have been reported, these do not provide adequate results in high aspect ratio structures.[69–72] To achieve good conformality, a self-limiting technique is required. The most commonly used is atomic layer deposition (ALD). The conformality originates from self-limiting surface reactions that are separated in time. A typical drawback therefore is the slow deposition rate, but novel ALD concepts such as spatial ALD (s-ALD) are aiming at significantly reducing process time and cost.[73,74]

Already quite a number of SSE materials have been deposited by ALD. A summary of these with their most relevant battery properties can been found in Table 3. The list immediately shows that different electrolytes can be deposited by ALD, however, this remains largely limited to the ternary oxides. Quaternary oxides like Li-La-Zr-O[75] (LLZO) or Li-La-Ti-O[76] (LLTO) can be deposited, however they did not show any ionic conductivity. In addition, the table shows the predicted stability window of the respective electrolyte material based on the calculations by Richards et al..[77] This to illustrate the clear tradeoff between conductivity and stability that often needs to be made. Note that the high conductivities achieved in single crystal or particle-based systems are so far not shown in ALD deposited materials. Finally, the table also lists the conformality of the ALD process (in the form of step coverage) when it has been reported in the original publication. The step coverage (in %) is calculated here based on the thickness deposited on the bottom of the pillar or trench divided by that at the top. Using this table, we will look in more depth at some of the most interesting materials deposited recently.

One of the solid electrolyte materials that has received quite some ALD attention recently is LiPON (nitrogen-doped lithium phosphate). LiPON was first discovered in 1990 at Oak Ridge national labs and is currently the most commonly used thin film solid electrolyte material[78] thanks to its wide electrochemical stability (0 to 5V vs Li$^+$/Li), low electronic leakage (<10^{-14} S cm^{-1}),[78,79] moderate ionic conductivity (10^{-6} S cm^{-1}) and the possibility to scale it down to nanometer thicknesses while maintaining good insulating properties.[79] Typically, the material is deposited by RF-sputtering, but recently also became available through ALD. Both CVD[80] and ALD[81,82] of Li$_3$PO$_4$ were already

available, but nitrogen doping of the material remained cumbersome. Although Li_3PO_4 is also a solid electrolyte, its conductivity is significantly lower than that of LiPON.[78,79] In addition, its stability is inferior to that of LiPON. Nitrogen incorporation in LiPON improves stability by forming, amongst others, Li_3N in a self-limiting reaction when in contact with lithium metal. In addition, it reduces the phosphate chain length and as such improves Li-ion conductivity.

Two different routes for ALD LiPON were discovered simultaneously, namely thermal[83] and plasma enhanced ALD.[84] The thermal ALD of LiPON was enabled by ensuring the attachment of nitrogen to the phosphate group in the same precursor (DEPA or diethyl phosphoramidate) which yielded LiPON through reaction with lithium bis(trimethylsilyl)amide (LiHMDS).[83] The resulting films had a conductivity of 6.6×10^{-7} S cm^{-1} at 25°C with an activation energy of 0.55 eV. The main advantage of this process is the good uniformity due to the usage of a thermal ALD process. However, this process suffered from silicon and carbon impurities due to incomplete reactions from the LiHMDS precursor. The purity of the films has, however, improved quite a bit since its first publication.[85]

On the other hand, a plasma ALD route was also discovered through the combination of Li *tert*-butoxide (LiO^{t}Bu), water, TMP (trimethyl phosphate) and a nitrogen plasma.[84] A conductivity of about 6×10^{-7} S cm^{-1} at 25 °C is reported for this process. The conductivity is here seen to be tunable by the plasma exposure time. In later work it was shown that the N-content in the films can be controlled by the plasma power, in a similar fashion to the RF-sputter depositions.[86] In addition, plasma enables lower deposition temperatures (down to 100 °C) and reduces the amount of impurities in the film.[84,86] This might open the way for LiPON protectvive coatings on metallic lithium. However, the need for a plasma step makes it less straightforward to obtain conformal films.[86]

Recently, the combination of LiO^{t}Bu and DEPA was evaluated[32] and used in the first full 3D TFB (see below). The combination of DEPA and LiO^{t}Bu yielded layers with a stoichiometry of Li_2PO_2N (not considering carbon contamination), and was named lithium-phosphazene (LPZ) as the P/N ratio is always 1. With the current process, the LPZ retains around 10% of carbon impurities, although no detrimental effect of this has been shown so far. The LPZ material has a conductivity of 3.5×10^{-7} S cm^{-1} at 25 °C. Nearly perfect conformality was shown in trenches of aspect ratio 10.

LiPON has thus far clearly proven its value in the development and fabrication of 3D thin film batteries. However, some key issues remain as well; one of these is its reactivity with air, leading to the formation of Li_2CO_3 which adds a resistive component to the performance.[32,87] Another issue is its temperature stability; as LiPON is only a good conductor in its amorphous form, it cannot withstand high temperatures. High temperatures might be necessary for the crystallization of the final electrode, thus limiting the options for the final electrode.

Recently, a glassy Li_3BO_3–Li_2CO_3 (LBCO) electrolyte has been fabricated through ALD using ozone as reactant.[88] These layers showed a remarkable ionic conductivity of 2×10^{-6} S cm^{-1} at 25 °C. The novelty of this approach lays in the fact that an incomplete reaction of the precursor to Li_2CO_3 was used as a dopant in the layer, which enhanced the ionic conductivity, as furthermore confirmed by first principle calculations. In addition, an excellent conformality for this ALD process was shown using pillars with an aspect ratio of 13.

Both in the case of LiPON and in the case of LBCO an enhanced process is used (O_3 or N_2 plasma). Using these kinds of reactants allows a reduction of the process temperature and to obtain layers without impurities. However, this typically comes at the cost of conformality. This can be attributed to their high reactivity (and is therefore more pronounced in the case of the N_2 plasma compared to O_3);[89] their concentration decreases as one progresses further along a high aspect ratio trench. This will

result in incomplete reaction at the bottom of the trench compared to the top. A full discussion of these issues is outside the scope of this review and can be found in refs. [89–91].

The electrolytes discussed above were amorphous glassy materials. They have the highest conductivity of the electrolytes deposited by ALD, but more importantly, they do not require a high temperature step. Crystalline electrolytes like LLZO[92] or LLTO[93] typically crystallize above 800 °C. Clearly this would cause intermixing between other functional battery layers leading to a loss of functionality.

Table 3. Comparison of conformal ALD-based solid electrolytes described in literature. AR = aspect ratio. The stability window listed here is based on thermodynamic calculations reported by Richards et al. [77]

Electrolyte Material	Max Ionic conductivity (S/cm)	Calculated stability window (vs Li$^+$/Li)	Conformality shown	Type of ALD process	Ref.
LiNbO$_3$	6×10^{-8}	1.8 up to 4.2 V	On CNTs	Thermal	[94]
Li$_3$PO$_4$	3×10^{-8}	0.9 up to 4.1 V	-	Thermal	[81]
	-		-		[82]
LiPON	7×10^{-7}	0 up to 4.1 V	AR 8 (100%)	Thermal	[83]
	6×10^{-7}		AR 10		[32]
	6×10^{-7}		On CNTs	Plasma	[84]
	5×10^{-7}		AR 25 (85%)		[86]
LiTaO$_3$	2×10^{-8}	-	AR 300 (50 nm in pores)	Thermal	[95]
LLZO	-	0.1 up to 3.5 V	AR 30 (>95%)	Ozone	[75]
Li$_x$Si$_y$O$_z$	6×10^{-9} (at 30 °C)	-	-	Thermal	[96]
LiAlO$_2$	1×10^{-9}	0.2 up to 3.5 V	-	Thermal	[97]
	5×10^{-8}		AR 11 (70%)	Thermal	[98,99]
LLTO	-	-	-	Ozone	[76]
Li$_3$N	-	0 up to 0.5 V	-	Thermal	[100]
LiAlF$_4$	4×10^{-8}	1.1 up to 6.5 V	-	Thermal	[101]
LiF	10^{-12}	0 up to 6 V	-	Thermal	[101]
Li$_x$Al$_y$S	3×10^{-7}	-	-	Thermal	[102]
Li$_3$BO$_3$-Li$_2$CO$_3$	2×10^{-6}	-	AR 13 (99%)	Ozone	[88]
Li$_2$CO$_3$	-	-	-	Thermal	[103]
	10^{-10}	-	AR 25 (80%)	Thermal	[104]
	10^{-10}	-	AR 25 (82%)	Plasma	[104]

Towards full 3D thin-film batteries

A recent step towards a full 3D TFB was published by Létiche et al., who showed a 3D TiO_2 thin-film electrode coated with a Li_3PO_4 SSE film.[38] The structure and property of this 3D thin-film electrode is shown in Figure 8. The 3D substrate was a double microtube structure fabricated from a Si wafer using standard photolithography processing. An Al_2O_3-barrier was deposited on the Si microtubes, on top of which Pt was deposited to act as the current-collector. ALD was used to deposit both the TiO_2 and Li_3PO_4 films. The electrochemical properties showed one of the highest footprint capacities reported for a 3D thin-film electrode, with up to 370 $\mu Ah\ cm^{-2}$ at a rate of C/16. Unfortunately, applying a higher C-rate significantly decreased the accessible capacity, and only 20% was accessible at a rate of 2 C. The low rate-performance is likely a combination of the bad rate-performance of anatase TiO_2 that was used, together with the low ionic conductivity of the Li_3PO_4 SSE (i.e. ~$10^{-7}\ S\ cm^{-1}$).
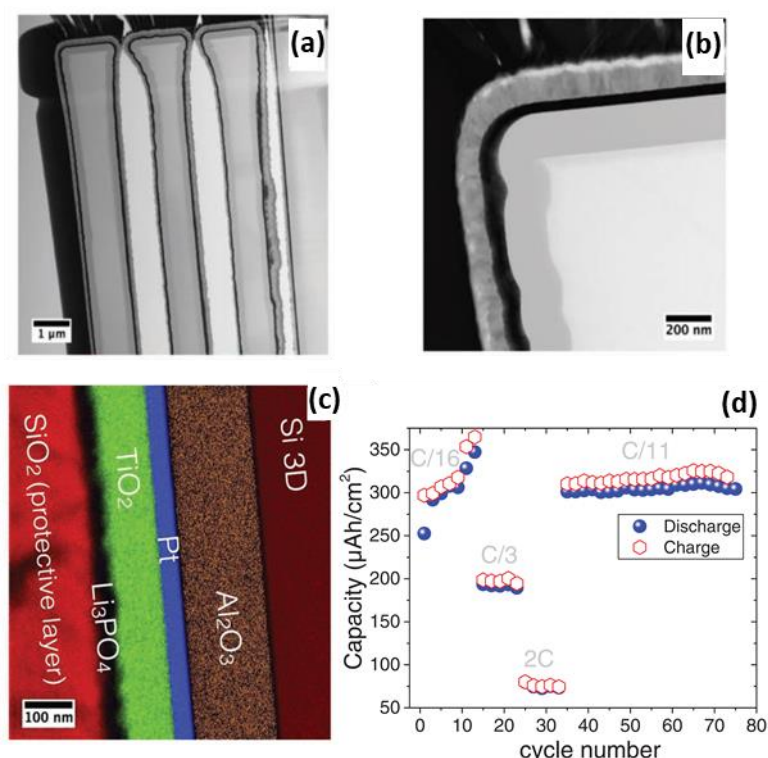

Figure 8. The structure and properties of a 3D TiO_2 thin-film electrode coated with a Li_3PO_4 SSE. (a-b) TEM micrographs of the coated microtube structure. (c) EDX-STEM images of the 3D thin-film stack. (d) Rate-performance of the 3D Li_3PO_4/TiO_2 electrode. Adapted with permission from [38]. Copyright 2019 Wiley.

The next major milestone was the fabrication of a full 3D TFB by Pearse et al., as shown in Figure 9.[46] All thin-film components were deposited using ALD. The 3D substrate was a periodic array of microholes etched in a silicon wafer. The 3D TFB consisted of 40 nm Ru (current collector), 70 nm prelithiated V_2O_5 (cathode), 50 nm LiPON (SSE), 10 nm SnN_x (anode), and 25 nm TiN (second current collector). Cu dots were deposited on top of the stack using electron beam deposition. These served as contacts to the underlying 3D TFB, and were used as a hard mask to define individual 3D TFB devices obtained after Ar^+ milling. Since no Li containing electrodes were deposited, a "prelihtiation" step was necessary to introduce lithium into V_2O_5 before subsequent deposition of the remaining layers. The SSE was Li_2PO_2N, a LiPON-analogue. The use of a thermal ALD process ensured that a conformal film could be achieved and that internal shorts were prevented.

The cycle stability the 3D TFB was assessed for planar and 3D TFBs (AEF = 4 and 10). The initial footprint capacity was about 30 $\mu Ah\ cm^{-2}$ (AEF = 10) at a current density of 100 $\mu A\ cm^{-2}$ (≈3 C) of which about

18

60% was retained after 100 cycles. This capacity retention can be considered high as an alloying anode (i.e. SnN$_x$) was used. It is possible that using an insertion-type anode would improve the cycle stability. The rate-performance was also tested, and about 15% of the capacity was accessible at an impressive current density of 10 mA cm^{-2} (≈300 C). These results showed for the first time the possibility of make 3D TFBs, and the feasibility of using ALD as a fabrication technique for the whole TFB stack. Unfortunately, the footprint capacity is still almost a factor 10 lower than for planar thin film batteries due to the sub-100 nm thin films.
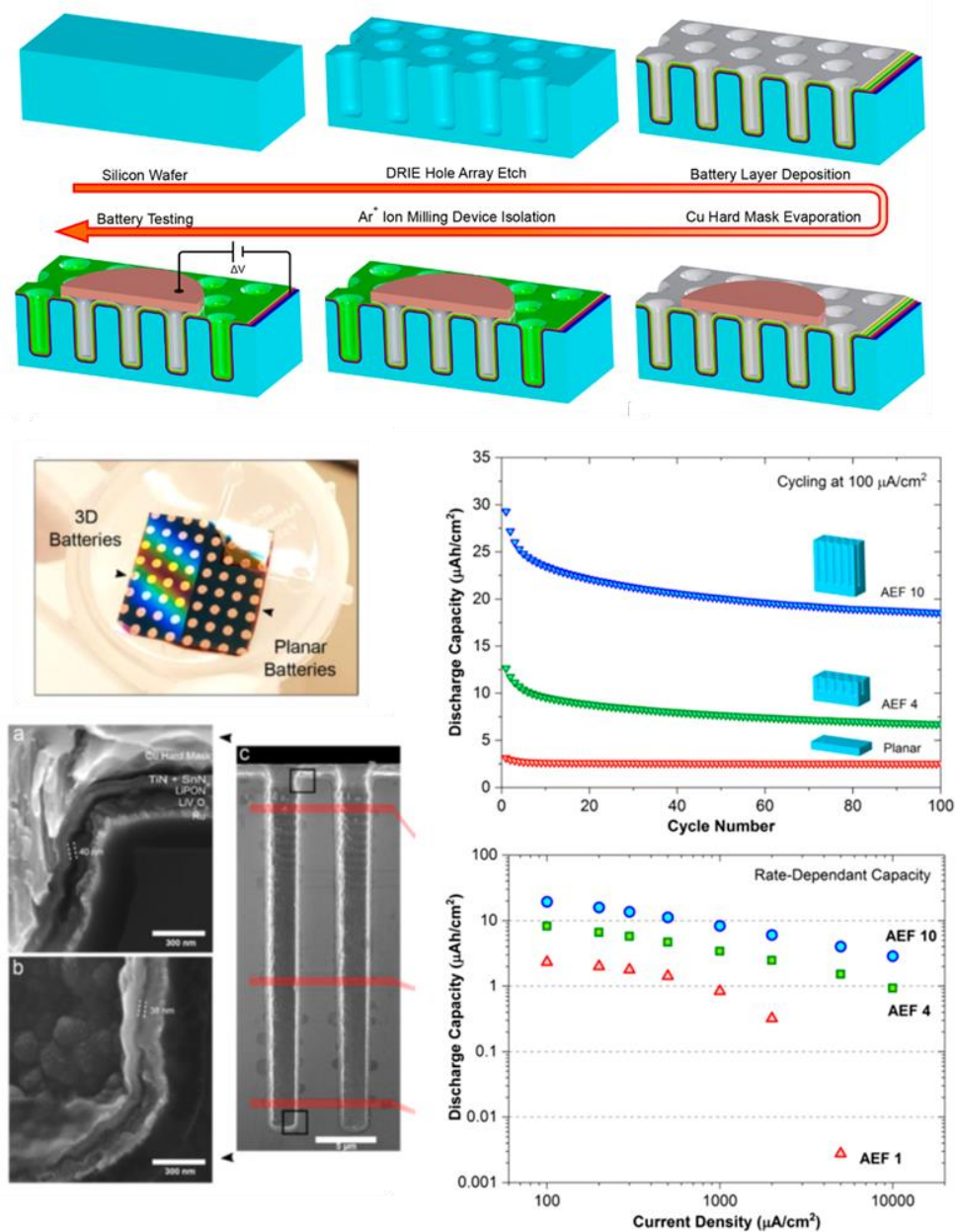

Figure 9. A 3D thin-film battery deposited in microholes etched into a Si wafer. A schematic of fabrication route is shown on the top. The full stack consists of Ru, V$_2$O$_5$, LiPON, SnN$_x$ + TiN, and Cu films. A picture of Si wafer comprising the 3D TFB microhole arrays (center left). Cross-section SEM micrographs of the full battery stack (bottom left). The electrochemical cycling stability (center right) and rate-performance (bottom right) of two 3D TFBs (AEF = 4 and 10) and a planar TFB (center right). Adapted with permission from [46]. Copyright 2019 American Chemical Society.

19

Conclusion

In this review we have explored the properties and promises of 3D TFBs. Derivations to calculate an optimal 3D arrangement based on micropillar arrays were shown. The various components needed to come to a full 3D TFB were discussed and state-of-the art 3D cathodes, anodes and SSEs were reviewed. Only until recently has there been a breakthrough in fabricating a full 3D TFB. By combining advanced microfabrication and gas-phase deposition techniques, a proof-of-concept 3D TFB was demonstrated.

The promise of 3D TFBs is a high footprint capacity with fast charging capability. Unfortunately, this potential has yet to be unlocked, as the highest reported capacity of a full cell is still a factor 2 to 10 lower than what commercial planar thin-film batteries can provide. To improve this, the use of optimized designs with thicker electrodes (or higher AEF) will be necessary. This includes tuning the AEF to the requirements of the electrode and SSE thickness. The next challenge is to obtain full 3D thin-film batteries with footprint capacities above 250 $\mu Ah\ cm^{-2}$ with stable and fast charging capabilities. Considering that, in a half-cell configuration, 3D thin-film cathodes with 500 $\mu Ah\ cm^{-2}$ and anodes with capacities near 200 $\mu Ah\ cm^{-2}$ have already been shown, such a task should be feasible in the near future. Note that the anode films are measured as the first or inner electrode. When the same thickness is deposited as outer electrode (with much wider effective pillar radius at that stage in the integration), the capacity will actually be near that of the cathode already.

In terms of integration, the compatibility of the various materials will need to be matched. Especially the SSE will be a crucial component to further optimize. Conformal and pinhole-free SSE layers with high ionic conductivity (e.g. above 10^{-7} S cm^{-2}) will need to be developed. Furthermore, an aspect to consider is the thermal stability of the thin-film materials. Many electrode materials are active in their crystalline form (e.g. $LiCoO_2$) which often require annealing temperatures above 500 °C to become active. This can lead to considerable changes (e.g. phase transitions, oxidation, etc.) to the underlying layers, which in turn leads to degradation and potentially internal shorts of the battery. Therefore, the outer electrode should preferably have a low temperature budget, especially when deposited over LiPON glass thin film. For this reason, amorphous materials such as the Cl-doped amorphous TiO_2 are of interest. ALD has been shown as a viable route to deposit all components needed to fabricate a full 3D TFB. Relatively "mild" conditions can be used to fabricate the electrodes and the solid-electrolyte. Nevertheless, improvements in the chemistry and properties of the active components will be required to improve the performance of 3D TFBs.

Finally, the development of cost-efficient and scalable fabrication techniques is necessary. At present, only a limited number of 3D TFBs have been shown in a lab environment. Significant developments will be necessary to reliably fabricate large number of functional 3D TFBs, for example, on Si-wafers or on foils. Techniques that can both address the issue of conformal deposition and cost-efficient fabrication need to be developed. Efforts such as using spatial ALD for the fabrication of 3D TFB components—which can potentially be used in a roll-to-roll production line—offer a route towards large-scale production. Alternatively, electrochemical deposition, or the combination of chemical solution deposition with ultrasonic spray coating might also offer interesting alternatives. Ultimately, a multidisciplinary effort in materials development and microfabrication techniques will be needed to obtain viable 3D TFB.

References

[1] A. Yoshino, in *Lithium-Ion Batter.* (Ed.: G. Pistoia), Elsevier, Amsterdam, **2014**, pp. 1–20.

[2] Internet Society, "The Internet of Things (IoT): An Overview," **2015**.

[3] Y. Khan, A. E. Ostfeld, C. M. Lochner, A. Pierre, A. C. Arias, *Adv. Mater.* **2016**, *28*, 4373.

[4] F. R. Fan, W. Tang, Z. L. Wang, *Adv. Mater.* **2016**, *28*, 4283.

[5] K. G. Gallagher, P. A. Nelson, in *Lithium-Ion Batter.* (Ed.: G. Pistoia), Elsevier, Amsterdam, **2014**, pp. 97–126.

[6] M. S. Leite, D. Ruzmetov, Z. Li, L. A. Bendersky, N. C. Bartelt, A. Kolmakov, A. A. Talin, *J. Mater. Chem. A* **2014**, *2*, 20552.

[7] A. E. Ostfeld, A. M. Gaikwad, Y. Khan, A. C. Arias, *Sci. Rep.* **2016**, *6*, 26122.

[8] S. Ferrari, M. Loveridge, S. D. Beattie, M. Jahn, R. J. Dashwood, R. Bhagat, *J. Power Sources* **2015**, *286*, 25.

[9] J. Song, W. West, in *Handb. Solid State Batter.* (Eds.: N.J. Dudney, W.C. West, J. Nanda), World Scientific, **2015**, pp. 591–627.

[10] M. Roberts, P. Johns, J. Owen, D. Brandell, K. Edstrom, G. El Enany, C. Guery, D. Golodnitsky, M. Lacey, C. Lecoeur, H. Mazor, E. Peled, E. Perre, M. M. Shaijumon, P. Simon, P.-L. Taberna, *J. Mater. Chem.* **2011**, *21*, 9876.

[11] G. W. Rubloff, A. C. Kozen, S. Bok Lee, *J. Vac. Sci. Technol. A Vacuum, Surfaces, Film.* **2013**, *31*, 058503.

[12] J. H. Pikul, H. Gang Zhang, J. Cho, P. V Braun, W. P. King, *Nat. Commun.* **2013**, *4*, 1732.

[13] N. Nitta, F. Wu, J. T. Lee, G. Yushin, *Mater. Today* **2014**, *18*, 252.

[14] J. M. Tarascon, M. Armand, *Nature* **2001**, *414*, 359.

[15] A. V. Churikov, A. V. Ivanishchev, A. V. Ushakov, V. O. Romanova, *J. Solid State Electrochem.* **2014**, *18*, 1425.

[16] Y. Sun, N. Liu, Y. Cui, *Nat. Energy* **2016**, *1*, 16071.

[17] P. M. Vereecken, C. Huyghebaert, *ECS Trans.* **2013**, *58*, 111.

[18] P. H. L. Notten, F. Roozeboom, R. a. H. Niessen, L. Baggetto, *Adv. Mater.* **2007**, *19*, 4564.

[19] M. Kurttepeli, S. Deng, F. Mattelaer, D. J. Cott, P. Vereecken, J. Dendooven, C. Detavernier, S. Bals, *ACS Appl. Mater. Interfaces* **2017**, *9*, 8055.

[20] D. J. Cott, M. Verheijen, O. Richard, I. Radu, S. De Gendt, S. Van Elshocht, P. M. Vereecken, *Carbon N. Y.* **2013**, *58*, 59.

[21] H. Xia, Q. Xia, B. Lin, J. Zhu, J. K. Seo, Y. S. Meng, *Nano Energy* **2016**, *22*, 475.

[22] S. Moitzheim, J. E. Balder, P. Poodt, S. Unnikrishnan, S. De Gendt, P. M. Vereecken, *Chem. Mater.* **2017**, *29*, 10007.

[23] S. Moitzheim, C. S. Nimisha, S. Deng, D. J. Cott, C. Detavernier, P. M. Vereecken, *Nanotechnology* **2014**, *25*, 504008.

[24] B. L. Ellis, P. Knauth, T. Djenizian, *Adv. Mater.* **2014**, *26*, 3368.

[25] K. Gerasopoulos, E. Pomerantseva, M. McCarthy, A. Brown, C. Wang, J. Culver, R. Ghodssi, *ACS Nano* **2012**, *6*, 6422.

[26] E. Eustache, P. Tilmant, L. Morgenroth, P. Roussel, G. Patriarche, D. Troadec, N. Rolland, T. Brousse, C. Lethien, *Adv. Energy Mater.* **2014**, *4*, 1301612.

[27] T. Dobbelaere, F. Mattelaer, J. Dendooven, P. Vereecken, C. Detavernier, *Chem. Mater.* **2016**, *28*, 3435.

[28] J. Xie, J. F. M. Oudenhoven, D. Li, C. Chen, R.-A. Eichel, P. H. L. Notten, *J. Electrochem. Soc.* **2016**, *163*, A2385.

[29] J. F. M. Oudenhoven, L. Baggetto, P. H. L. Notten, *Adv. Energy Mater.* **2011**, *1*, 10.

[30] T. Dobbelaere, F. Mattelaer, A. K. Roy, P. Vereecken, C. Detavernier, *J. Mater. Chem. A* **2017**, *5*, 330.

[31] V. Cremers, F. Geenen, C. Detavernier, J. Dendooven, *J. Vac. Sci. Technol. A Vacuum, Surfaces, Film.* **2017**, *35*, 01B115.

[32] A. J. Pearse, T. E. Schmitt, E. J. Fuller, F. El-Gabaly, C. F. Lin, K. Gerasopoulos, A. C. Kozen, A. A. Talin, G. Rubloff, K. E. Gregorczyk, *Chem. Mater.* **2017**, *29*, 3740.

[33] B. Put, P. M. Vereecken, N. Labyedh, A. Sepulveda, C. Huyghebaert, I. P. Radu, A. Stesmans, *ACS Appl. Mater. Interfaces* **2015**, *7*, 22413.

[34] S. Moitzheim, J. E. Balder, R. Ritasalo, S. Ek, P. Poodt, S. Unnikrishnan, S. De Gendt, P. M. Vereecken, *ACS Appl. Energy Mater.* **2019**, *2*, 1774.

[35] E. J. Van Den Ham, S. Gielis, M. K. Van Bael, A. Hardy, *ACS Energy Lett.* **2016**, *1*, 1184.

[36] M. Y. Timmermans, N. Labyedh, F. Mattelaer, S. P. Zankowski, S. Deheryan, C. Detavernier, P. M. Vereecken, **2017**, *164*, D954.

[37] N. Labyedh, B. Put, A.-A. El Mel, P. M. Vereecken, *J. Electrochem. Soc.* **2018**, *165*, B3184.

[38] M. Létiche, E. Eustache, J. Freixas, A. Demortière, V. De Andrade, L. Morgenroth, P. Tilmant, F. Vaurette, D. Troadec, P. Roussel, T. Brousse, C. Lethien, *Adv. Energy Mater.* **2017**, *7*, 1601402.

[39] N. J. Dudney, Y. Jang, *J. Power Sources* **2003**, *119–121*, 300.

[40] H. J. Noh, S. Youn, C. S. Yoon, Y. K. Sun, *J. Power Sources* **2013**, *233*, 121.

[41] S. Moitzheim, S. de Gendt, P. M. Vereecken, *J. Electrochem. Soc.* **2019**, *166*, A1.

[42] K. B. Gandrud, A. Pettersen, O. Nilsen, H. Fjellvåg, *J. Mater. Chem. A* **2013**, *1*, 9054.

[43] F. Mattelaer, K. Geryl, G. Rampelberg, J. Dendooven, C. Detavernier, *ACS Appl. Mater. Interfaces* **2017**, *9*, 13121.

[44] M. M. Shaijumon, E. Perre, B. Daffos, P. L. Taberna, J. M. Tarascon, P. Simon, *Adv. Mater.* **2010**, *22*, 4978.

[45] F. Mattelaer, K. Geryl, G. Rampelberg, T. Dobbelaere, J. Dendooven, C. Detavernier, *RSC Adv.* **2016**, *6*, 114658.

[46] A. Pearse, T. Schmitt, E. Sahadeo, D. M. Stewart, A. Kozen, K. Gerasopoulos, A. A. Talin, S. B. Lee, G. W. Rubloff, K. E. Gregorczyk, *ACS Nano* **2018**, *12*, 4286.

[47] N. Labyedh, M. Y. Timmermans, F. Mattelaer, M. J. Mees, C. Detavernier, P. M. Vereecken, in *Meet. Abstr. Electrochem. Soc.*, **2016**, p. 1605.

22

[48] N. Labyedh, M. Y. Timmermans, P. M. Vereecken, in *Meet. Abstr. Electrochem. Soc.*, **2017**, p. 585.

[49] Y. Zargouni, S. Deheryan, A. Radisic, K. Alouani, P. M. Vereecken, *Nanomaterials* **2017**, *7*, 126.

[50] F. Mattelaer, P. M. Vereecken, J. Dendooven, C. Detavernier, *Chem. Mater.* **2015**, *27*, 3628.

[51] M. Park, X. Zhang, M. Chung, G. B. Less, A. M. Sastry, *J. Power Sources* **2010**, *195*, 7904.

[52] S. Chugh, R. Mehta, N. Lu, F. D. Dios, M. J. Kim, Z. Chen, *Carbon N. Y.* **2015**, *93*, 393.

[53] L. Baggetto, R. a. H. Niessen, F. Roozeboom, P. H. L. Notten, *Adv. Funct. Mater.* **2008**, *18*, 1057.

[54] L. Baggetto, H. C. M. Knoops, R. a. H. Niessen, W. M. M. Kessels, P. H. L. Notten, *J. Mater. Chem.* **2010**, *20*, 3703.

[55] A. Kim, E. Park, H. Lee, H. Kim, *J. Alloys Compd.* **2016**, *681*, 301.

[56] V. Augustyn, J. Come, M. a Lowe, J. W. Kim, P.-L. Taberna, S. H. Tolbert, H. D. Abruña, P. Simon, B. Dunn, *Nat. Mater.* **2013**, *12*, 518.

[57] B. Xu, D. Qian, Z. Wang, Y. S. Meng, *Mater. Sci. Eng. R Reports* **2012**, *73*, 51.

[58] J. Xu, X. Wang, X. Wang, D. Chen, X. Chen, D. Li, G. Shen, *ChemElectroChem* **2014**, *1*, 975.

[59] W. Zeng, F. Zheng, R. Li, Y. Zhan, Y. Li, J. Liu, *Nanoscale* **2012**, *4*, 2760.

[60] S. K. Cheah, E. Perre, M. Rooth, M. Fondell, A. Hårsta, L. Nyholm, M. Boman, T. Gustafsson, J. Lu, P. Simon, K. Edström, *Nano Lett.* **2009**, *9*, 3230.

[61] M. Valvo, M. Roberts, G. Oltean, B. Sun, D. Rehnlund, D. Brandell, L. Nyholm, T. Gustafsson, K. Edström, *J. Mater. Chem. A* **2013**, *1*, 9281.

[62] J. Xie, P. P. R. M. L. Harks, D. Li, L. H. J. Raijmakers, P. H. L. Notten, *Solid State Ionics* **2016**, *287*, 83.

[63] V. Subramanian, A. Karki, K. I. Gnanasekar, F. P. Eddy, B. Rambabu, *J. Power Sources* **2006**, *159*, 186.

[64] X. Yan, Z. Wang, M. He, Z. Hou, T. Xia, G. Liu, X. Chen, *Energy Technol.* **2015**, *3*, 801.

[65] V. Miikkulainen, O. Nilsen, M. Laitinen, T. Sajavaara, H. Fjellvåg, *RSC Adv.* **2013**, *3*, 7537.

[66] K. Knapas, A. Rahtu, M. Ritala, *Langmuir* **2010**, *26*, 848.

[67] M. Mattinen, P. J. King, L. Khriachtchev, M. J. Heikkilä, B. Fleming, S. Rushworth, K. Mizohata, K. Meinander, J. Räisänen, M. Ritala, M. Leskelä, *Mater. Today Chem.* **2018**, *9*, 17.

[68] A. Manthiram, X. Yu, S. Wang, *Nat. Rev. Mater.* **2017**, *2*, 16103.

[69] F. Xu, N. J. Dudney, G. M. Veith, Y. Kim, C. Erdonmez, W. Lai, Y. M. Chiang, *J. Mater. Res.* **2010**, *25*, 1507.

[70] D. Ruzmetov, V. P. Oleshko, P. M. Haney, H. J. Lezec, K. Karki, K. H. Baloch, A. K. Agrawal, A. V. Davydov, S. Krylyuk, Y. Liu, J. Huang, M. Tanase, J. Cumings, A. A. Talin, *Nano Lett.* **2012**, *12*, 505.

[71] J. Xie, J. F. M. Oudenhoven, P.-P. R. M. L. Harks, D. Li, P. H. L. Notten, *J. Electrochem. Soc.* **2015**, *162*, A249.

[72] T. Fujibayashi, Y. Kubota, K. Iwabuchi, N. Yoshii, *AIP Adv.* **2017**, *7*, 085110.

23

[73] P. S. Maydannik, T. O. Kääriäinen, K. Lahtinen, D. C. Cameron, M. Söderlund, P. Soininen, P. Johansson, J. Kuusipalo, L. Moro, X. Zeng, *J. Vac. Sci. Technol. A Vacuum, Surfaces, Film.* **2014**, *32*, 051603.

[74] P. Poodt, D. C. Cameron, E. Dickey, S. M. George, V. Kuznetsov, G. N. Parsons, F. Roozeboom, G. Sundaram, A. Vermeer, *J. Vac. Sci. Technol. A Vacuum, Surfaces, Film.* **2012**, *30*, 010802.

[75] E. Kazyak, K. H. Chen, K. N. Wood, A. L. Davis, T. Thompson, A. R. Bielinski, A. J. Sanchez, X. Wang, C. Wang, J. Sakamoto, N. P. Dasgupta, *Chem. Mater.* **2017**, *29*, 3785.

[76] T. Aaltonen, M. Alnes, O. Nilsen, L. Costelle, H. Fjellvåg, *J. Mater. Chem.* **2010**, *20*, 2877.

[77] W. D. Richards, L. J. Miara, Y. Wang, J. C. Kim, G. Ceder, *Chem. Mater.* **2016**, *28*, 266.

[78] X. Yu, *J. Electrochem. Soc.* **1997**, *144*, 524.

[79] B. Put, P. M. Vereecken, J. Meersschaut, A. Sepúlveda, A. Stesmans, *ACS Appl. Mater. Interfaces* **2016**, *8*, 7060.

[80] T. V. Vu, C. Park, *Solid State Ionics* **2017**, *313*, 14.

[81] B. Wang, J. Liu, Q. Sun, R. Li, T. Sham, X. Sun, *Nanotechnology* **2014**, *25*, 504007.

[82] J. Hämäläinen, J. Holopainen, F. Munnik, T. Hatanpää, M. Heikkilä, M. Ritala, M. Leskelä, *J. Electrochem. Soc.* **2012**, *159*, A259.

[83] M. Nisula, Y. Shindo, H. Koga, M. Karppinen, *Chem. Mater.* **2015**, *27*, 6987.

[84] A. C. Kozen, A. J. Pearse, C.-F. Lin, M. Noked, G. W. Rubloff, *Chem. Mater.* **2015**, *27*, 5324.

[85] M. Nisula, *Atomic/Molecular Layer Deposition of an All-Solid-State Thin-Film Battery Based on Organic Electrode Materials (Doctoral Dissertation)*, **2018**.

[86] B. Put, M. J. Mees, N. Hornsveld, S. Hollevoet, A. Sepúlveda, P. M. Vereecken, W. M. M. Kessels, M. Creatore, *J. Electrochem. Soc.* **2019**, *166*, A1239.

[87] C. S. Nimisha, G. M. Rao, N. Munichandraiah, G. Natarajan, D. C. Cameron, *Solid State Ionics* **2011**, *185*, 47.

[88] E. Kazyak, K. H. Chen, A. L. Davis, S. Yu, A. J. Sanchez, J. Lasso, A. R. Bielinski, T. Thompson, J. Sakamoto, D. J. Siegel, N. P. Dasgupta, *J. Mater. Chem. A* **2018**, *6*, 19425.

[89] H. C. M. Knoops, E. Langereis, M. C. M. van de Sanden, W. M. M. Kessels, *J. Electrochem. Soc.* **2010**, *157*, G241.

[90] J. Dendooven, D. Deduytsche, J. Musschoot, R. L. Vanmeirhaeghe, C. Detavernier, *J. Electrochem. Soc.* **2010**, *157*, G111.

[91] C. Detavernier, J. Dendooven, D. Deduytsche, J. Musschoot, **2008**, *16*, 239.

[92] Q. Liu, Z. Geng, C. Han, Y. Fu, S. Li, Y. bing He, F. Kang, B. Li, *J. Power Sources* **2018**, *389*, 120.

[93] J.-F. Wu, X. Guo, *Phys. Chem. Chem. Phys.* **2017**, *19*, 5880.

[94] B. Wang, Y. Zhao, M. N. Banis, Q. Sun, K. R. Adair, R. Li, T.-K. Sham, X. Sun, *ACS Appl. Mater. Interfaces* **2018**, *10*, 1654.

[95] J. Liu, M. N. Banis, X. Li, A. Lushington, M. Cai, R. Li, T.-K. K. Sham, X. Sun, *J. Phys. Chem. C* **2013**, *117*, 20260.

[96] B. Wang, J. Liu, M. Norouzi Banis, Q. Sun, Y. Zhao, R. Li, T. K. Sham, X. Sun, *ACS Appl. Mater.*

Interfaces **2017**, *9*, 31786.

[97]   Y. Hu, A. Ruud, V. Miikkulainen, T. Norby, O. Nilsen, H. Fjellvåg, *RSC Adv.* **2016**, *6*, 60479.

[98]   J. S. Park, X. Meng, J. W. Elam, S. Hao, C. Wolverton, C. Kim, J. Cabana, *Chem. Mater.* **2014**, *26*, 3128.

[99]   D. J. Comstock, J. W. Elam, *J. Phys. Chem. C* **2013**, *117*, 1677.

[100]   E. Østreng, P. Vajeeston, O. Nilsen, H. Fjellvåg, *RSC Adv.* **2012**, *2*, 6315.

[101]   J. Xie, A. D. Sendek, E. D. Cubuk, X. Zhang, Z. Lu, Y. Gong, T. Wu, F. Shi, W. Liu, E. J. Reed, Y. Cui, *ACS Nano* **2017**, *11*, 7019.

[102]   Y. Cao, X. Meng, J. W. Elam, *ChemElectroChem* **2016**, *3*, 858.

[103]   A. S. Cavanagh, Y. Lee, B. Yoon, S. George, in *ECS Trans.*, **2010**, pp. 223–229.

[104]   N. Hornsveld, B. Put, W. M. M. Kessels, P. M. Vereecken, M. Creatore, *RSC Adv.* **2017**, *7*, 41359.